

A New Airborne Laser-Induced Fluorescence Instrument for In Situ Detection of Formaldehyde throughout the Troposphere and Lower Stratosphere

M. Cazorla^{1,*}, G. M. Wolfe^{1,2}, S. A. Bailey¹, A. K. Swanson^{1,3}, H. L. Arkinson⁴, and T. F. Hanisco¹

[1]{Atmospheric Chemistry and Dynamics Lab, NASA Goddard Space Flight Center, Greenbelt, MD, USA}

[2]{Joint Center for Earth Systems Technology, University of Maryland Baltimore County, Baltimore, MD, USA}

[3]{Goddard Earth Sciences Technology and Research, University of Maryland Baltimore County, Baltimore, MD, USA}

[4]{Department of Atmospheric and Oceanic Science, University of Maryland, College Park, MD, USA}

[*]{Now at Universidad San Francisco de Quito, Instituto de Investigaciones Atmosféricas, Colegio de Ciencias e Ingeniería, Diego de Robles y Vía Interoceánica, Quito, Ecuador }

Correspondence to: T. F. Hanisco (thomas.hanisco@nasa.gov)

Abstract

The NASA In Situ Airborne Formaldehyde (ISAF) instrument is a high-performance laser-based detector for gas phase formaldehyde (HCHO). ISAF uses rotational-state specific laser excitation at 353 nm for laser-induced fluorescence (LIF) detection of HCHO. A number of features make ISAF ideal for airborne deployment, including 1) a compact, low-maintenance fiber laser, 2) a single-pass design for stable signal response, 3) a straightforward inlet design, and 4) a standalone data acquisition system. A full description of the instrument design is given, along with detailed performance characteristics. The accuracy of reported mixing ratios is $\pm 10\%$ based

on calibration against IR and UV absorption of a primary HCHO standard. Precision at 1 Hz is typically better than 20% above 100 pptv, with uncertainty in the signal background contributing most to variability at low mixing ratios. The 1 Hz detection limit for a signal/noise ratio of 2 is 36 pptv for 10 mW of laser power, and the e-fold time response at typical sample flow rates is 0.19 s. ISAF has already flown on several field missions and platforms with excellent results.

1 Introduction

Formaldehyde (HCHO) is a ubiquitous constituent of the Earth's atmosphere. It is primarily produced during hydrocarbon oxidation, with an estimated source strength of $250 \pm 54 \text{ Tg yr}^{-1}$ (Fortems-Cheiney et al., 2012). In the background troposphere, the oxidation of methane (CH_4) by hydroxyl radical (OH) is the main source. Photochemical degradation of anthropogenic and biogenic hydrocarbons greatly enhances HCHO production in the lower troposphere, with the most significant precursor being the biogenic hydrocarbon isoprene. HCHO is also emitted through fuel combustion (Olague et al., 2009; Luecken et al., 2012), biomass burning (Yokelson et al., 2013) and vegetation (DiGangi et al., 2011). These sources are generally minor globally compared to secondary production, but they may be significant locally. HCHO is lost via photolysis and reaction with OH, with a typical daytime lifetime of 2 – 3 hours. Wet and dry deposition are minor sinks globally, but can be significant locally, such as during precipitation. Typical mixing ratios range from 10's of pptv (parts per trillion by volume) in pristine air to several hundred ppbv (parts per billion by volume) near combustion sources.

HCHO is a tracer for, and active participant in, multiple atmospheric processes. As a byproduct of hydrocarbon oxidation, HCHO can provide quantitative constraints on the photochemical link between primary emissions and secondary pollutants (Chatfield et al., 2010; Duncan et al., 2010). A number of studies have employed satellite-based HCHO observations to better constrain isoprene emission inventories (Palmer et al., 2003; Palmer et al., 2006; Millet et al., 2008; Marais et al., 2012). Because of its short lifetime, the mixing ratio of HCHO in the upper troposphere is typically 10 to 100 times less than that near continental surfaces. Convection can pump surface air to the upper troposphere very rapidly, and HCHO is a valuable marker for the efficiency of this process (Barth et al., 2007; Fried et al., 2008) and a participant in ensuing chemistry (Apel et

Thomas Hanisco 11/13/2014 2:07 PM

Deleted:), but

Thomas Hanisco 11/13/2014 2:07 PM

Deleted: .

1 al., 2012). Furthermore, photolysis of HCHO is a potent source of radicals and thus helps to
2 propagate chemical cycles (Edwards et al., 2011; Edwards et al., 2013).

3 A handful of techniques are currently available to measure HCHO in the atmosphere; a review of
4 these methods and inter-comparisons can be found elsewhere (Gilpin, et al., 1997; Cardenas et
5 al., 2000; Hak et al., 2005; Wisthaler et al., 2008; Kaiser et al., 2014). Laser-based and
6 spectroscopic methods are generally employed when high sensitivity and time response are
7 required. The most common among these include tunable diode laser-based absorption
8 spectroscopy (Weibring et al., 2007; Fried, et al., 2008), differential optical absorption
9 spectroscopy (DOAS) (Baidar et al., 2013) and laser-induced fluorescence (LIF) (Hottle et al.,
10 2009). Diode laser spectroscopy and DOAS rely on molecular absorption in the IR and UV
11 regions, respectively, while LIF utilizes UV-stimulated emission. DOAS can be applied for in
12 situ or remote (column-averaged) observations, and a similar principle underlies satellite-based
13 HCHO observations (Chance et al., 2000). Indeed, HCHO is one of only a few hydrocarbons
14 observable from space, and high-quality *in situ* observations are critical for retrieval validation.

15 Instrumentation for airborne observations is held to stringent engineering standards. An ideal
16 instrument is small, lightweight, low power, and able to withstand vibrations and large
17 temperature variations. Low maintenance, calibration stability and fast time response (≥ 1 Hz) are
18 also desirable. For HCHO, a substantial dynamic range – roughly four orders of magnitude – is
19 also necessary to adequately sample mixing ratios throughout the troposphere and lower
20 stratosphere. Here, we present the NASA in situ airborne formaldehyde (ISAF) instrument, a new
21 LIF-based HCHO detector that meets or exceeds all of the above requirements. After a brief
22 synopsis of the LIF method in Section 2, we provide a detailed description of instrument
23 construction (Section 3) and performance characteristics (Section 4). Section 5 gives an example
24 of observations taken during a recent field campaign.

25

26 2 Principle of operation

27 LIF is a well-established spectroscopic method for selective measurement of trace gases. LIF
28 detection of HCHO was first reported by Becker et al. (1975) and refined by Möhlmann (1985).
29 Hottle et al. (2009) applied the technique to in-situ atmospheric measurements. In these

Thomas Hanisco 11/13/2014 2:07 PM

Deleted: TDLAS) (

Thomas Hanisco 11/13/2014 2:07 PM

Deleted: TDLAS

Thomas Hanisco 11/13/2014 2:07 PM

Deleted: high

1 approaches a tunable laser is used to ensure specificity to HCHO and a pulsed operation is used
2 to minimize background noise. Figure 1 illustrates the key processes involved. A narrow-band
3 laser, tuned to a specific rovibronic absorption line in the 353 – 355 nm region ~~of the $A - X$~~
4 electronic transition, promotes a fraction of the HCHO molecules to the first excited electronic
5 state. The majority of these excited HCHO molecules are quenched back to the ground electronic
6 state by collisions with air. A small fraction (~1%) undergo vibrational relaxation and
7 subsequently relax to the ground electronic state through fluorescence, emitting a structured band
8 of photons in the range of 400 – 470 nm (Becker et al., 1975; Shibuya et al., 1979; Mohlmann,
9 1985). Fluorescence occurs with an exponential decay over several hundred nanoseconds (Fig. 1,
10 right). The number of fluorescence photons per unit laser power is proportional to the mixing
11 ratio of HCHO in the sample gas. This relationship is readily quantified with a known standard.

12 For ISAF, the chosen absorption feature is centered at 353.163 nm, which has a cross section of
13 $3.77 \times 10^{-19} \text{ cm}^2$ at 150 Torr (Co et al., 2005). While this cross section is ~7% lower than the peak
14 value in this band, it is chosen because of the presence of several unique adjacent peaks, notably
15 a triplet feature (see Fig. 6). This area of the spectrum serves as a “fingerprint” for HCHO,
16 simplifying the wavelength-tracking algorithm. The offline position is only 0.005 nm away from
17 the peak. This wavelength difference provides a high differential cross-section for HCHO, but
18 the differential is negligible for species that have non-structured absorptions in this region. This
19 allows for precise and selective measurements of HCHO. To date, we have not identified any
20 interfering species that has a measurable differential absorption and fluorescence between the on-
21 and offline positions.

22

23 **3 Instrument description**

24 ISAF is comprised of four main subsystems: a UV fiber laser, an optical bench comprising the
25 detection and reference cells, gas handling components (pressure controller, inlet system, tubing,
26 valves and pump), and the data acquisition computer. Each of these subsystems is described in
27 greater detail below. Aside from the vacuum pump, all components are contained in a single
28 custom-built chassis with dimensions of 60 cm length x 43 cm width x 35 cm height. The layout
29 of the chassis is shown in Figure 2. This chassis is designed to run on 28VDC, which is supplied

Thomas Hanisco 11/13/2014 2:07 PM

Deleted: oft he

directly from aircraft power or through an external AC/DC interface unit. The instrument itself weighs 25 kg and draws 200W. An external pump, computer, and control box are used for operation on larger aircraft with on-board operators. Including all peripherals, the total instrument package weighs 60 kg and draws a peak power of 600 W.

3.1 Laser

Pulsed, tunable UV laser radiation is provided by a NovaWave (now Thermo Scientific) TFL 3000 fiber laser. The laser uses a master oscillator power amplifier architecture to provide narrow wavelength, tunable, pulsed light at 353 nm. A single distributed feedback laser operating at 1060 nm is chopped with an acousto-optic modulator and amplified in two stages to 2 W with a series of diode-pumped, semiconductor-doped, polarization-maintaining optical fibers. The 1060 nm output is fiber-coupled into a harmonic generation module containing two periodically poled non-linear crystals and collimating optics. The harmonic generation housing is mounted on the optical bench (Figure 2) and coupled with free-space optics. The repetition rate is 300 kHz, with a pulse width of 25 ns and a typical output power of 10 – 40 mW. The output wavelength is tunable to ~ 0.0001 nm, permitting resolution of individual rovibronic absorption features. Computer control is provided via RS232. The entire unit weighs ~ 12 kg and draws < 60 W, making it an attractive alternative to larger laser systems typically used for LIF.

3.2 Optical bench

The optical bench is shown in greater detail in Figures 3 and 4. The bench is an aluminum sandwich panel with 1.25 cm thick honeycomb core and with 0.1 cm cladding. The bench is mounted to the instrument chassis with vibration damping mounts (Sorbothane) to minimize vibrations. Figure 3 shows the optical bench and the path of the laser. Figure 4 shows a cross-sectional view of the detection cell. The simplicity and single-laser pass design of this system is a major advantage for field applications; alignment rarely degrades throughout flight campaigns or during shipping. Likewise, the instrument shows no effects in high vibration environments or in aircraft maneuvers. Both cells are heated to a constant temperature of 35 °C, and capability exists to heat other parts of the instrument if needed (i.e. for high-altitude applications).

1 UV laser light is collimated at 2 mm diameter at the output of the harmonic stage with a lens
2 (Thor LA4600-UV, $f = 100$ mm) and directed to the detection cell via four dielectric-coated
3 mirrors (Edmund 47-323). Two of these mirrors, along with the two between the detection and
4 reference cells, utilize piezo-driven mounts (Newport Agilis) for remote alignment. The laser
5 beam enters and exits the reduced-pressure detection cell (Figure 4) through V-type anti-
6 reflection (VAR) coated silica windows (Edmund 48-207) tilted at 5° to redirect reflections from
7 the window surfaces out of the beam propagation path. The arms of the detection cell contain a
8 series of circular baffles with 2.5 – 3.5 mm apertures to eliminate stray light. Baffles and cell
9 walls are coated with a combination of Avian black paint (Avian Technologies), black anodize,
10 and molybdenum oxide treated aluminum (Insta-Black 380, EPI). The innermost baffles are
11 coated with an ultra-black custom carbon nanotube treatment (Hagopian, 2011). The laser beam,
12 gas flow and focus of the collection lens intersect orthogonally in the center of the cell. Along
13 this detection axis, photons are imaged with an aspheric lens (Edmund 6-321) through a 370 nm
14 long pass absorption filter (Edmund 66-049) and a 400 nm long pass interference filter (Omega
15 3RD400LP). The image is partially focused with another lens (Thor LA1608, $f = 75$ mm) onto a
16 photomultiplier tube (PMT) (Hamamatsu 7360). A spherical mirror (Thor CM254, $f = 25$ mm) is
17 located opposite the aspheric lens to improve collection efficiency.

18 After the detection cell, a beam sampler (Thor BSF05-UV) diverts $\sim 4\%$ of the laser to a power
19 monitor comprised of a diffuser (Thor DGUIV10-600), filter (Thor FGUV11) and amplified
20 photodiode (OSI 555-UV). The photodiode has a large active area (1 cm^2) to ensure that the
21 entire laser beam is detected. The diffuser is needed to spread the laser over enough of the
22 photodiode to avoid inhomogeneities in the photodiode responsivity. The main laser beam is
23 directed into a reference cell (Fig. 3, lower right), which is used to monitor the laser wavelength.
24 This cell is nearly identical to the sample cell shown in Figure 4; the main differences are shorter
25 arms and a neutral density filter (Thor NE30A) to limit fluorescence signal intensity. A heated
26 cartridge filled with powdered ureaformaldehyde glue (DAP Weldwood) provides a large
27 concentration of HCHO ($\sim 1\text{ ppmv}$). This cell is static (no gas flow) but is maintained at the same
28 pressure as the sample cell by coupling the arms to the sample cell exhaust. This is critical for
29 maintaining the same absorption line width in both cells, as the reference cell signal is used to
30 correct sample cell data (see Sec. 3.5). A normally-closed solenoid valve and an activated

Thomas Hanisco 11/13/2014 2:07 PM
Deleted: The main

Thomas Hanisco 11/13/2014 2:07 PM
Deleted: .

1 charcoal scrubber are placed inline to limit sample cell contamination. The laser beam is
2 ultimately dumped into a second power monitor, which is primarily used to gauge laser
3 alignment.

4 3.3 Gas handling

5 The primary components of the air sampling system include the aircraft inlet, pressure controller,
6 and vacuum pump. Some care must be taken with the inlet system to minimize adsorption and
7 production/loss of HCHO on surfaces (Wert et al., 2002). Outgassing of HCHO from tubing
8 walls, physisorption and desorption of HCHO, and the chemical or catalytic conversion of
9 oxygenated hydrocarbons on metal surfaces to HCHO are primary concerns in the design of the
10 sampling system. Fast flows, low surface area fluorocarbon or fluorocarbon-coated surfaces, and
11 minimal dead space are the design features. For example, there are no valves or sensors between
12 the tip of the inlet and the instrument; the sampling path is continuous tubing with VCO
13 (Swagelok) fittings. Furthermore, all metal surfaces are coated with fluorocarbon (fluoropel,
14 Cytonix), tubing is PTFE or FEP, and pressure, temperature, and flow are measured after the
15 detection cell.

16 Figure 5 depicts the inlet design used on the NASA DC-8 aircraft. The inlet tube is a 45 cm
17 length of 0.48 cm ID silicosteel (Restek) coated with fluoropel mounted at 90° to the airflow to
18 reject particles. The tip of the inlet is chamfered at 15° to enhance the particle rejection and is
19 heated to 30 – 60 °C inside the winglet to prevent condensation and sticking. A tapered
20 aluminum nacelle oriented parallel to the direction of flight serves as a flow straightener and
21 generates a ram pressure equal to ~1.15 times that of ambient at the inlet tip, driving an air flow
22 of 10 – 25 slm through the inlet. The corresponding volumetric flow at typical pressures and
23 temperatures is 25 – 65 L min⁻¹. Inside the aircraft, air is carried via 1 m of 0.7 cm ID PTFE
24 tubing to the instrument chassis and is sub-sampled at 2 – 4 slm. The excess flow passes through
25 a flow meter (Honeywell) and exits behind the inlet. The residence time in the heated silicosteel
26 portion of the tube is 8 – 20 ms, with an additional 35 – 100 ms in the transfer tubing.

27 Inside the chassis, sample air passes through a pressure controller (MKS 640A) heated to 35 °C,
28 followed by a ~20 cm length of 0.4 cm ID PFA tubing connected to the detection cell. The
29 residence time in the detection cell is ~115 ms. Sample pressure, temperature and flow rate are

Thomas Hanisco 11/13/2014 2:07 PM

Deleted: oxegenated

Thomas Hanisco 11/13/2014 2:07 PM

Deleted: ,

1 monitored immediately downstream of the cell. A small amount of sample air (~100 sccm) is
2 drawn through the laser arms to reduce contamination from painted surfaces or dead space.
3 Sample air is exhausted through the vacuum pump (Agilent IDP-3 or Vacuubrand MD-1). During
4 instrument shutdown, contamination is minimized by backfilling the cell with ambient air
5 scrubbed by a Drierite/molecular sieve cartridge, which reduces HCHO to < 100 pptv.

6 3.4 Data acquisition

7 All hardware interfacing is handled with an all-solid state CompactRIO (National Instruments)
8 with real-time operating system and a field programmable gate array (FPGA). The FPGA and
9 acquisition software are configured for fast photon counting and autonomous operation. Six 200
10 MHz counters are used to integrate PMT signals at a nominal rate of 10 Hz. Pulses from the
11 sample cell PMT are sampled by three of these counters, one non-gated (continuous), and two
12 each with a separate gate (Fig. 1, right). The “full” gate samples both scattered laser light and
13 HCHO fluorescence, while the “delayed” gate excludes the laser. The reference cell gate is the
14 same width as the full gate. Laser power is also monitored at 10 Hz. Other diagnostics (laser
15 parameters, temperatures, pressures, flows, GPS and aircraft data) are recorded at 1 Hz.

16 Figure 6 illustrates the standard data acquisition routine. Online counting is done for 2.5 s
17 (25 points), followed by 0.5 s (5 points) offline. Laser drift (mainly due to temperature of the
18 seed laser diode) requires an active line-locking algorithm. The online position is alternately
19 shifted to a slightly (± 0.0001 nm) lower or higher wavelength on adjacent online cycles, and the
20 reference cell is monitored for maximum signal. When the laser is tuned precisely to the online
21 position the reference cell is at the maximum signal. When the laser is tuned 0.0001 nm (or
22 0.0002 nm) off of the peak position the signal drops by about ~5% (or ~10%). The resulting
23 small changes in the reference cell signal are used to maintain the laser on the peak of the line.
24 The signal is also used to correct the sample signal by the ~5% (or ~10%) needed to normalize
25 the signal to the signal at the peak position.

26 Once per hour, a full scan over the HCHO fingerprint is recorded. This is primarily used to
27 optimize the harmonic generation crystal temperatures and as a performance diagnostic. For
28 example, the presence of interfering species can be detected in the spectrum. To date, we have
29 not detected any features other than those shown in Figure 6. This is not surprising. To be

Thomas Hanisco 11/13/2014 2:07 PM
Deleted: inside

Thomas Hanisco 11/13/2014 2:07 PM
Deleted: The resulting small changes in absorption in the sample cell are removed during data reduction (see below).

detected, the potential species must absorb at 353.163 nm, fluoresce in the 400 – 470 nm band, and have a significant fluorescence lifetime.

3.5 Data reduction

Both the full and delay gate signals can be used to derive HCHO mixing ratios. The delay gate excludes ~53% of the fluorescence signal, but it is also relatively insensitive to laser scatter (from Raman, Rayleigh or particulates) and gives superior signal/noise ratios below ~550 pptv HCHO. Thus, the delay gate signal is typically used, and all results discussed below stem from this signal. The full gate data provides a useful metric for scatter and other potential laser-related issues.

The detected signal is proportional to the abundance of HCHO and the laser power. To first order, we can determine HCHO from the ratio of the laser power-normalized difference between the online and offline signals and the calibration factor. To minimize systematic noise, however, we use additional steps to convert raw counts to mixing ratios. These analysis steps are 1) normalization by laser power; 2) background subtraction, determined by a smoothed interpolation of offline signals; 3) normalization by the reference cell signal to account for deviations from the maximum absorption wavelength due to the line-locking algorithm; and 4) application of a pressure-dependent calibration factor (see Sec. 4.1).

4 Performance

4.1 Sensitivity

Detection sensitivity (signal response per unit HCHO) is a function of laser power, collection efficiency, PMT response and counter gating. As mentioned above, signals are normalized by laser power. Because of the single-pass design, laser alignment does not affect sensitivity except in extreme cases when the laser is partially blocked. In practice the laser maintains alignment for entire field campaigns and usually during shipments to and from deployment locations. During flight, the ratio of the two power monitors (at the exits of the detection and reference cells) is constant to $\pm 3\%$.

1 Collection efficiency depends on the physical characteristics of the sample cell, including the
2 types of collection optics (lenses and filters) and their relative spacing. We do not expect the
3 collection efficiency to change under normal operation. However, catastrophic events, such as the
4 degradation of optics from contamination could reduce the sensitivity. The responsivity of the
5 PMT should be stable ~~in the short term (months to years)~~, but it can degrade over the lifetime of
6 the PMT. The gated counter timing is a fixed parameter and is optimized for signal/noise.
7 Changes in the gate timing relative to the laser pulse could affect the sensitivity. These changes
8 are easily diagnosed in data reduction and can be corrected by using the non-delayed gates.

9 In practice, instrument sensitivity is determined via calibration against a primary standard,
10 consisting of a 500 – 700 ppbv mixture of HCHO in N₂ (Scott Gas/Air Liquide). This mixture is
11 calibrated every few months (typically before and after a field deployment) with an MKS
12 Multigas 2031 Fourier transform infrared spectrometer using manufacturer-provided IR cross
13 sections tied to gravimetric permeation tube calibrations. The 1 σ uncertainty in mixing ratio from
14 any single determination is typically 2 – 3%. HCHO mixtures are also stable over time; for
15 example, five calibrations performed on a single tank over the course of a year give a mixing
16 ratio of 611 \pm 8 ppbv and show no trend.

17 To better constrain the calibration to literature standards, a series of experiments were performed
18 to compare concentrations derived from FTIR and long-path UV absorption. The UV absorption
19 cell was a custom-built, 200 cm long, 1.1 cm diameter stainless steel tube fitted with windows,
20 gas ports and a pressure gauge. Visible light from a Cathodeon deuterium lamp was filtered
21 (Edmund U-330) and focused through the cell and measured with an Ocean Optics Maya 2000
22 spectrometer. The cell was held above atmosphere (1110 – 1150 Torr) with a gas flow rate of 6
23 slm. Absorption measurements were carried out simultaneously in both the IR and UV systems
24 using a high concentration (nominally 11 ppmv) HCHO standard. Literature UV cross sections
25 (Meller and Moortgat, 2000) in the 285 – 370 nm range were fit to the measured absorption
26 spectra (nominal resolution \sim 1 nm) to obtain HCHO concentrations and mixing ratios. Based on
27 11 such experiments, the mixing ratios from UV and IR are 10.49 \pm 0.20 ppmv and 10.96 \pm 0.02
28 ppmv, respectively. The ratio of UV/IR = 0.9571 is applied to all IR-derived values; for example,
29 the IR-derived average mixing ratio of 611 ppbv is corrected to 585 ppbv. By making this

Thomas Hanisco 11/13/2014 2:07 PM

Deleted: ,

1 adjustment, our calibration is tied to the Meller and Moorgat (2000) cross section rather than the
2 MKS spectrometer.

3 Calibrations of ISAF are achieved via standard additions to zero air. Zero air is delivered either
4 from an ultra-zero air cylinder or from a zero air generator (Sabio 2020) with an additional
5 Drierite/molecular sieve scrubber to reduce HCHO mixing ratios to 30 pptv or less. Small flows
6 of the primary HCHO standard (1 – 50 sccm) are diluted into a 5 slm flow of zero air to yield
7 HCHO concentrations in the range of 0 – 5 ppbv. Signal is plotted against the diluted HCHO
8 mixing ratio, and the slope of this relationship gives the instrument sensitivity (see inset of Fig.
9 7). This sensitivity varies with sample cell pressure due to the combined effects of number
10 density, absorption line broadening, and quenching. Figure 7 shows this pressure dependence as
11 determined from a number of standard addition experiments. Peak sensitivity occurs at a cell
12 pressure of 200 mbar. In flight, the system is configured to maintain a constant pressure that is
13 dictated by the ceiling of the aircraft. For example, on the NASA DC-8, the cell pressure is
14 typically held at 100 mbar, and the sensitivity is $75 \text{ counts s}^{-1} \text{ mW}^{-1} \text{ ppbv}^{-1}$. Propagation of
15 uncertainties in the HCHO concentration, determined by both the absolute UV absorption
16 measurement and dilution flow rates, gives an estimated accuracy of $\pm 10\%$.

17 Calibrations are generally carried out in the laboratory both before and after field missions.
18 Because HCHO adheres to surfaces in tubing, fittings, regulators and flow meters, several days
19 are needed to ensure consistent results, especially with new PTFE or FEP tubing. Calibrations
20 can be performed in the field during campaigns, if needed. In practice, these calibrations are used
21 to monitor instrument performance. We have never changed the instrument sensitivity calibration
22 numbers during a campaign. Based on 4 field campaigns spanning 2 years, sensitivity varies by
23 less than 10% over a single mission and by less than 30% between missions. Given the difficulty
24 of adding a known amount of HCHO, it is likely that the sensitivity of the instrument was
25 constant over those two years and that the variability in the calibrations is due to differences in
26 calibration conditions and personnel.

27 4.2 Precision

28 The instrument precision is primarily limited by processes that generate noise or affect the
29 background (offline) signal. The largest potential sources of noise, Rayleigh and Raman

Thomas Hanisco 11/13/2014 2:07 PM
Deleted: .

1 scattering of laser light, are reduced with a combination of optical filters, absorbing surfaces (e.g.
2 baffles) and gated photon counting. Laboratory tests indicate that scattering contributes less than
3 7 counts s⁻¹ mW⁻¹ to the background signal at 100 mbar.

4 Figure 8 shows the short-term precision estimated from the normalized standard deviation
5 ($\sigma_x/\langle x \rangle$) for data segments of 10 to 15 minutes at a range of constant mixing ratios. Also
6 displayed is the inverse square root dependence expected from Poisson counting statistics. Above
7 mixing ratios of ~100 pptv, the precision is better than 20% and exhibits the expected slope but is
8 somewhat higher than the Poisson limit. Some fraction of this offset is due to uncertainty in the
9 background. This would also explain the reduced precision observed at the lowest mixing ratios.
10 It is also likely that some “extra” variability is contributed by the calibration gas addition system,
11 which would be directly proportional to the HCHO mixing ratio. We note that small changes in
12 room temperature can cause small fluctuations in the amount of HCHO added to the calibration
13 gas flow, presumably from increased or decreased desorption of HCHO from surfaces (i.e.
14 regulator, valves, flow meters, and fittings). The true instrument precision thus lies between the
15 measured and predicted values in Figure 8.

16 In theory, time-averaging will improve instrument precision. Figure 9 shows the mean-
17 normalized Allen deviation for 60 minutes of sampling at a constant mixing ratio of 5.1 ppbv. At
18 short averaging times, precision improves as the inverse square root of integration time,
19 consistent with white noise as the dominant source of variability. Averaging from the native data
20 rate of 0.1 s to the typical reporting interval of 1 s improves precision by a factor of 3. Averaging
21 to the “optimal” interval of 130 s improves precision by a factor of 18, although natural
22 variability would likely dominate on this timescale in the real atmosphere.

23 4.3 Detection limit

24 For counting statistics, the signal-to-noise ratio is defined as:

$$\frac{S}{N} = \frac{pC_f[HCHO]t}{\sqrt{pC_f[HCHO]t + 2pBt}} \quad (1)$$

25 Where p is laser power, C_f is the calibration factor (sensitivity), $[HCHO]$ is the mixing ratio, B is
26 the background count rate and t is the integration time. For a typical laser power of 10 mW, a

1 sensitivity of $75 \text{ counts s}^{-1} \text{ mW}^{-1} \text{ ppbv}^{-1}$, a background count rate of $8 \text{ counts s}^{-1} \text{ mW}^{-1}$, and an
2 integration time of 1 s, the estimated detection limit is 18 pptv for $S/N = 1$ or 36 pptv for $S/N = 2$.
3 This value agrees well with the 1σ variability of 17 pptv observed at low mixing ratios (inset of
4 Fig. 8). Time averaging will improve the detection limit in proportion to the precision (Fig. 9).
5 The detection limit scales as the inverse square root of laser power. The laser is capable of
6 producing as much as 40 mW of power, thus ISAF can potentially achieve a factor of two
7 reduction in the detection limit by operating at higher laser power. For example, the instrument
8 operated at 20 mW during its first deployment and achieved higher S/N . More recently, however
9 we choose to operate at reduced power (10 mW) to extend the life of the laser diodes and non-
10 linear crystals.

11 The inset of Figure 8 is a typical example of the signal measured with zero air added to the
12 calibration system. Zero air and ultra zero air have 20 – 50 pptv HCHO, but we can obtain lower
13 values by passing the air through a molecular sieve. With clean FEP or PFA tubing,
14 measurements of zero or near zero are easily obtained, even after exposure to 10 or 20 ppbv of
15 HCHO. The ISAF instrument has no measurable chemical offset or bias of HCHO and shows
16 little if any “memory” of exposure to high concentrations of HCHO (see sections 4.4 and 4.5 for
17 more detail). However, the uncertainty shown in the inset of Figure 8 is typical at these low
18 concentrations. At very low fluorescence photon count rates, small changes in the laser scatter
19 between the online and offline position can lead to an offset in the measurement. This is because
20 we assume that the laser scatter is equal at the online and offline wavelengths. Though the
21 wavelength difference is small (0.005 nm) there is some laser pointing change due to walk-off in
22 the harmonic generation stage between these wavelengths, and potentially a small difference in
23 laser scatter. This difference can result in a negative or positive offset. We assign an uncertainty
24 of ± 10 pptv to account for this potential offset.

25 4.4 Time response

26 Though the nominal sampling frequency is 10 Hz, the flush time of sampling volumes can limit
27 the effective instrument time response. Minimizing the response time is critical for applications
28 that require measurements of fast changes in concentration, such as eddy covariance and
29 sampling of discrete plumes, and for eliminating contamination from exposure to high

Thomas Hanisco 11/13/2014 2:07 PM
Deleted: .

concentrations of HCHO. For typical inlet pressures and flow rates, the plug-flow transit time from the tip of the inlet to the instrument chassis is 43 – 120 ms. This creates a delay between sampling and detection but should not cause significant “smearing” of concentration fluctuations, as the flow is typically turbulent ($Re \sim 3000 - 6000$). Such smearing can, however, occur in the pressure controller and sample cell. Based on the internal cell volume of 60 cm^3 and a typical volumetric flow rate of 31 L min^{-1} (2.75 slm at 100 mbar and 35°C), the expected 1/e cell flush time is 115 ms. Figure 10 shows the instantaneous response to a 10 ms pulse of HCHO, delivered via a fast switching valve (IEP series, The Lee Company). The observed decay time is 190 ms, somewhat slower than that predicted from flow characteristics. The extra delay is likely due to the pressure controller, which acts as a critical orifice and adds to the internal volume of the sampling system. A faster time response can be achieved by increasing the flow rate through the sample cell, which depends on the conductance of the pressure controller and the pumping speed.

The fast time response is an important feature contamination-free detection at low concentrations of HCHO. HCHO continuously adsorbs and desorbs from surfaces inside the instrument sampling system. This reversible process can lead to biases, especially when low concentrations are sampled after exposure of the instrument to very high concentrations. The effects of reversible adsorption and desorption of HCHO from surfaces is minimized by having a large mass flow, small volumes and low surface area, the same features that lead to the fast time response. The measured time response includes both the effects of volumetric displacement and adsorption/desorption. The impact on in situ measurements is demonstrated in Section 4.5.

4.5 Field demonstration

As of March 2014, ISAF has flown successfully on four field missions spanning three platforms and a wide range of chemical conditions. For many of these flights, the instrument has flown autonomously, without an operator. Figure 11 presents observations from a single flight on the NASA DC-8 during the Deep Convective Clouds and Chemistry (DC3) experiment, which took place over the central U.S. in May and June 2012 (Barth et al., submitted). On this flight, the DC-8 sampled at altitudes of 0 – 12 km, with HCHO mixing ratios ranging from 50 – 5500 pptv. The expanded views in Fig. 11 show a boundary layer leg and an upper tropospheric leg to illustrate the time response, dynamic range and sensitivity of ISAF. During DC3, ISAF was flown

1 simultaneously with a well-established instrument, the U. Colorado DFGAS (Difference
2 Frequency Generation Absorption Spectrometer) (Weibring et al., 2007). Preliminary analysis
3 indicates excellent agreement between these two instruments, and a rigorous inter-comparison
4 will be the subject of a future publication.

5 The time response of the instrument in flight is illustrated in Figure 12. These data were obtained
6 during the Studies of Emissions and Atmospheric Composition, Clouds and Climate Coupling
7 Regional Surveys (SEAC4RS) campaign in 2013. During this flight on August 26, 2012, the
8 DC8 sampled the smoke plume from the Ring fire in Yosemite National Park as it passed from
9 California to Nevada. In this plume, measured at a constant pressure altitude of 5km, the HCHO
10 abundance reached over 200 ppbv. The data is shown in linear and log scale to illustrate the
11 several orders of magnitude change in HCHO during this segment. The observations
12 demonstrate the ability of ISAF to measure low concentrations of HCHO even after exposure to
13 very high concentrations for several minutes.

14 The expanded views provide 50 second snapshots of two regions where the abundance of HCHO
15 is highly variable. The 10 Hz data is shown along with the 1 Hz data to demonstrate the fast
16 response of the instrument. These 10 Hz data show much more structure than the 1 Hz and at the
17 edges of plume filaments the transitions are much steeper. For example, the edge of the plume at
18 time = 40 s in Figures 12 b and c drops from an abundance of 65 ppb to 25 ppb (1/e) in 0.3 s. If
19 this were limited by instrument response alone, that is if the plume were to have an abrupt
20 boundary, the corresponding instrument time constant would be 0.3 s. Several filaments have
21 steeper edges, near 0.2 s, while most show broader edges that indicate more diffuse boundaries.
22 These steep edges are consistent with the ISAF time response of around 0.2 s shown in Figure
23 10. These examples – fast time response and the ability to measure highly variable concentrations
24 – are important demonstrations of the small effect of the reversible adsorption and desorption of
25 HCHO in the ISAF inlet and instrument. The reversible adsorption and desorption clearly are
26 factors because the time constant is larger than the volumetric flush time, but the effects are
27 small, on the order 100 ms.

1 **5 Summary**

2 The NASA ISAF instrument is a compact, high-sensitivity, field-proven instrument for airborne
3 observations of HCHO throughout the troposphere and lower stratosphere. The instrument
4 capabilities are summarized in Table 1. Already, it has flown on the NASA DC-8, the NOAA
5 WP-3D and the NCAR G-V aircraft on four aircraft field campaigns: DC3, Southeast Nexus
6 | (SENEX), SEAC4RS, and CONvective Transport of Active Species in the Tropics
7 | (CONTRAST). Future work will include modifications for deployment on high-altitude aircraft,
8 such as the NASA ER-2 or WB-57, to achieve an even more complete observational dataset.

9

10 **Acknowledgements**

11 This research was funded by the Goddard Internal Research and Development (IRAD) program
12 and the NASA ROSES grant NNH10ZDA001N-SEAC4RS. The NASA Postdoctoral Program
13 provided funding for M. Cazorla.

14

Thomas Hanisco 11/13/2014 2:07 PM

Deleted: Studies of Emissions and Atmospheric Composition, Clouds and Climate Coupling Regional Surveys (

Thomas Hanisco 11/13/2014 2:07 PM

Deleted:),

1 **References**

- 2 Apel, E. C., et al.,: Impact of the deep convection of isoprene and other reactive trace species on
3 radicals and ozone in the upper troposphere, *Atmos. Chem. Phys.*, 12, 1135-1150, 10.5194/acp-
4 12-1135-2012, 2012.
- 5 Baidar, S., Oetjen, H., Coburn, S., Dix, B., Ortega, I., Sinreich, R., and Volkamer, R.: The CU
6 Airborne MAX-DOAS instrument: vertical profiling of aerosol extinction and trace gases,
7 *Atmos. Meas. Tech.*, 6, 719-739, 10.5194/amt-6-719-2013, 2013.
- 8 Barth, M. C., Cantrell, C. A., Brune, W. H., Rutledge, S. A., Crawford, J. H., Huntrieser, H.,
9 Carey, L. D., MacGorman, D., Weisman, M., Pickering, K. E., Bruning, E., Anderson, B., Apel,
10 E., Biggerstaff, M., Campos, T., Campuzano-Jost, P., Cohen, R. C., Crounse, J. D., Day, D. A.,
11 Diskin, G., Flocke, F., Fried, A., Garland, C., Heikes, B., Honomichi, S., Hornbrook, R., Huey,
12 L. G., Jimenez, J., Lang, T., Lichtenstern, M., Mikoviny, T., O'Sullivan, D., Pan, L., Peischl, J.,
13 Pollack, I., Rierner, D., Ryerson, T., Schlager, H., St. Clair, J. M., Walega, J., Weibring, P.,
14 Weinheimer, A., Wennberg, P. O., Wisthaler, A., Wooldridge, P. J., Ziegler, C.: The deep
15 convective clouds and chemistry (DC3) field campaign, *J. Geophys. Res. A.*, submitted.
- 16 Barth, M. C., Kim, S. W., Skamarock, W. C., Stuart, A. L., Pickering, K. E., and Ott, L. E.:
17 Simulations of the redistribution of formaldehyde, formic acid, and peroxides in the 10 July 1996
18 Stratospheric-Tropospheric Experiment: Radiation, Aerosols, and Ozone deep convection storm,
19 *J. Geophys. Res.-Atmos.*, 112, D13310, 10.1029/2006jd008046, 2007.
- 20 Becker, K. H., Schurath, U., and Tatarczyk, T.: Fluorescence determination of low formaldehyde
21 concentrations in air by dye laser excitation, *Appl. Optics*, 14, 310-313, 10.1364/ao.14.000310,
22 1975.
- 23 Cardenas, L. M., Brassington, D. J., Allan, B. J., Coe, H., Alicke, B., Platt, U., Wilson, K. M.,
24 Plane, J. M. C., and Penkett, S. A.: Intercomparison of formaldehyde measurements in clean and
25 polluted atmospheres, *J. Atmos. Chem.*, 37, 53-80, 10.1023/a:1006383520819, 2000.
- 26 Chance, K., Palmer, P. I., Spurr, R. J. D., Martin, R. V., Kurosu, T. P., and Jacob, D. J.: Satellite
27 observations of formaldehyde over North America from GOME, *Geophys. Res. Lett.*, 27, 3461-
28 3464, 10.1029/2000gl011857, 2000.

Thomas Hanisco 11/13/2014 2:07 PM

Deleted: . et al.,:

1 Chatfield, R. B., Ren, X., Brune, W., and Schwab, J.: Controls on urban ozone production rate as
2 indicated by formaldehyde oxidation rate and nitric oxide, *Atmos. Environ.*, 44, 5395-5406, 2010.

3 Co, D. T., Hanisco, T. F., Anderson, J. G., and Keutsch, F. N.: Rotationally resolved absorption
4 cross sections of formaldehyde in the 28100-28500 cm⁻¹ (351-356 nm) spectral region:
5 Implications for in situ LIF measurements, *J. Phys. Chem. A*, 109, 10675-10682,
6 10.1021/jp053466i, 2005.

7 DiGangi, J. P., Boyle, E. S., Karl, T., Harley, P., Turnipseed, A., Kim, S., Cantrell, C., Maudlin
8 III, R. L., Zheng, W., Flocke, F., Hall, S. R., Ullmann, K., Nakashima, Y., Paul, J. B., Wolfe, G.
9 M., Desai, A. R., Kajii, Y., Guenther, A., and Keutsch, F. N.: First direct measurements of
10 formaldehyde flux via eddy covariance: implications for missing in-canopy formaldehyde
11 sources, *Atmos. Chem. Phys.*, 11, 10565-10578, 2011.

12 Duncan, B., Yoshida, Y., Olson, J., Sillman, S., Martin, R., Lamsal, L., Hu, Y., Pickering, K.,
13 Retscher, C., Allen, D., and Crawford, J.: Application of OMI observations to a space-based
14 indicator of NO_x and VOC controls on surface ozone formation, *Atmos. Environ.*, 44, 2213-
15 2223, 10.1016/j.atmosenv.2010.03.010, 2010.

16 Edwards, P., Evans, M. J., Commane, R., Ingham, T., Stone, D., Mahajan, A. S., Oetjen, H.,
17 Dorsey, J. R., Hopkins, J. R., Lee, J. D., Moller, S. J., Leigh, R., Plane, J. M. C., Carpenter, L. J.,
18 and Heard, D. E.: Hydrogen oxide photochemistry in the northern Canadian spring time boundary
19 layer, *J. Geophys. Res.-A*, 116, 10.1029/2011jd016390, 2011.

20 Edwards, P. M., Young, C. J., Aikin, K., deGouw, J., Dube, W. P., Geiger, F., Gilman, J.,
21 Helmig, D., Holloway, J. S., Kercher, J., Lerner, B., Martin, R., McLaren, R., Parrish, D. D.,
22 Peischl, J., Roberts, J. M., Ryerson, T. B., Thornton, J., Warneke, C., Williams, E. J., and Brown,
23 S. S.: Ozone photochemistry in an oil and natural gas extraction region during winter: simulations
24 of a snow-free season in the Uintah Basin, Utah, *Atmos. Chem. Phys.*, 13, 8955-8971,
25 10.5194/acp-13-8955-2013, 2013.

26 Fortems-Cheiney, A., Chevallier, F., Pison, I., Bousquet, P., Saunio, M., Szopa, S., Cressot, C.,
27 Kurosu, T. P., Chance, K., and Fried, A.: The formaldehyde budget as seen by a global-scale
28 multi-constraint and multi-species inversion system, *Atmos. Chem. Phys.*, 12, 6699-6721,
29 10.5194/acp-12-6699-2012, 2012.

- 1 Fried, A., [Olson, J. R., Walega, J. G., Crawford, J. H., Chen, G., Weibring, P., Richter, D.,](#)
- 2 [Roller, C., Tittel, F., Porter, M., Fuelberg, H., Halland, J., Bertram, T. H., Cohen, R. C.,](#)
- 3 [Pickering, K., Heikes, B. G., Snow, J. A., Shen, H., O'Sullivan, D. W., Brune, W. H., Ren, X.,](#)
- 4 [Blake, D. R., Blake, N., Sachse, G., Diskin, G. S., Podolske, J., Vay, S. A., Shetter, R. E., Hall, S.](#)
- 5 [R., Anderson, B. E., Thornhill, L., Clarke, A. D., McNaughton, C. S., Singh, H. B., Avery, M. A.,](#)
- 6 [Huey, G., Kim, S., and Millet, D. B.:](#) Role of convection in redistributing formaldehyde to the
- 7 upper troposphere over North America and the North Atlantic during the summer 2004 INTEX
- 8 campaign, *J. Geophys. Res. A*, 113, 10.1029/2007jd009760, 2008.
- 9 [Gilpin, T., Apel, E., Fried, A., Wert, B., Calvert, J., Genfa, Z., Dasgupta, P. Harder, J. W.,](#)
- 10 [Heikes, B., Hopkins, B., Westberg, H., Kleindienst, Lee, Y-N., Zhou, X., Lonneman, W., and](#)
- 11 [Sewell, S.:](#) Intercomparison of six ambient CH₂O measurement techniques, *J. Geophys. Res. A*,
- 12 [102, 21161 - 21188, 1997.](#)
- 13 Hagopian, J.: Carbon nanotubes for stray light suppression, Art. 9417, NASA Tech. Briefs, 2011.
- 14 Hak, C., Pundt, I., Trick, S., Kern, C., Platt, U., Dommen, J., Ordonez, C., Prevot, A. S. H.,
- 15 Junkermann, W., Astorga-Llorens, C., Larsen, B. R., Mellqvist, J., Strandberg, A., Yu, Y., Galle,
- 16 B., Kleffmann, J., Lorzer, J. C., Braathen, G. O., and Volkamer, R.: Intercomparison of four
- 17 different in-situ techniques for ambient formaldehyde measurements in urban air, *Atmos. Chem.*
- 18 *Phys.*, 5, 2881-2900, 2005.
- 19 Hottle, J. R., Huisman, A. J., Digangi, J. P., Kammrath, A., Galloway, M. M., Coens, K. L., and
- 20 Keutsch, F. N.: A Laser Induced Fluorescence-Based Instrument for In-Situ Measurements of
- 21 Atmospheric Formaldehyde, *Environ. Sci. Tech.*, 43, 790-795, 2009.
- 22 Kaiser, J., Li, X., Tillmann, R., Acir, I., Rohrer, F., Wegener, R., and Keutsch, F. N.:
- 23 Intercomparison of Hantzsch and fiber-laser-induced-fluorescence formaldehyde measurements,
- 24 *Atmos. Meas. Tech.*, 7, 233-255, 10.5194/amtd-7-233-2014, 2014.
- 25 Luecken, D. J., Hutzell, W. T., Strum, M. L., and Pouliot, G. A.: Regional sources of atmospheric
- 26 formaldehyde and acetaldehyde, and implications for atmospheric modeling, *Atmos. Environ.*,
- 27 47, 477-490, 10.1016/j.atmosenv.2011.10.005, 2012.
- 28 Marais, E. A., Jacob, D. J., Kurosu, T. P., Chance, K., Murphy, J. G., Reeves, C., Mills, G.,
- 29 Casadio, S., Millet, D. B., Barkley, M. P., Paulot, F., and Mao, J.: Isoprene emissions in Africa

1 inferred from OMI observations of formaldehyde columns, *Atmos. Chem. Phys.*, 12, 6219-6235,
2 10.5194/acp-12-6219-2012, 2012.

3 Meller, R., and Moortgat, G. K.: Temperature dependence of the absorption cross sections of
4 formaldehyde between 223 and 323 K in the wavelength range 225-375 nm, *J. Geophys. Res. A*,
5 105, 7089-7101, 10.1029/1999jd901074, 2000.

6 Millet, D. B., Jacob, D. J., Boersma, K. F., Fu, T. M., Kurosu, T. P., Chance, K., Heald, C. L.,
7 and Guenther, A.: Spatial distribution of isoprene emissions from North America derived from
8 formaldehyde column measurements by the OMI satellite sensor, *J. Geophys. Res. A*, 113,
9 10.1029/2007jd008950, 2008.

10 Mohlmann, G. R.: Formaldehyde detection in air by laser-induced fluorescence, *Applied*
11 *Spectroscopy*, 39, 98-101, 10.1366/0003702854249088, 1985.

12 Olaguer, E. P., Rappengluck, B., Lefer, B., Stutz, J., Dibb, J., Griffin, R., Brune, W. H., Shauck,
13 M., Buhr, M., Jeffries, H., Vizuete, W., and Pinto, J. P.: Deciphering the Role of Radical
14 Precursors during the Second Texas Air Quality Study, *J. Air Waste Manage. Assoc.*, 59, 1258-
15 1277, 10.3155/1047-3289.59.11.1258, 2009.

16 Palmer, P. I., Jacob, D. J., Fiore, A. M., Martin, R. V., Chance, K., and Kurosu, T. P.: Mapping
17 isoprene emissions over North America using formaldehyde column observations from space, *J.*
18 *Geophys. Res. A*, 108, [4180](#), 10.1029/2002jd002153, 2003.

19 Palmer, P. I., Abbot, D. S., Fu, T. M., Jacob, D. J., Chance, K., Kurosu, T. P., Guenther, A.,
20 Wiedinmyer, C., Stanton, J. C., Pilling, M. J., Pressley, S. N., Lamb, B., and Sumner, A. L.:
21 Quantifying the seasonal and interannual variability of North American isoprene emissions using
22 satellite observations of the formaldehyde column, *J. Geophys. Res. A*, 111, [D12315](#),
23 10.1029/2005jd006689, 2006.

24 Shibuya, K., Holtermann, D. L., Peacock, J. R., and Lee, E. K. C.: Fluorescence emission-
25 spectroscopy, radiative lifetimes, and vibrational-relaxation rates of the 40 and 41 single vibronic
26 levels of D2CO and HDCO (A1A2), *Journal of Physical Chemistry*, 83, 940-944,
27 10.1021/j100471a012, 1979.

1 Weibring, P., Richter, D., Walega, J. G., and Fried, A.: First demonstration of a high performance
2 difference frequency spectrometer on airborne platforms, Opt. Express, 15, 13476-13495,
3 10.1364/oe.15.013476, 2007.

4 Wert, B. P., Fried, A., Henry, B., and Cartier, S.: Evaluation of inlets used for the airborne
5 measurement of formaldehyde, J. Geophys. Res. A, 107, 10.1029/2001jd001072, 2002.

6 Wisthaler, A., Apel, E. C., Bossmeyer, J., Hansel, A., Junkermann, W., Koppmann, R., Meier, R.,
7 Muller, K., Solomon, S. J., Steinbrecher, R., Tillmann, R., and Brauers, T.: Technical Note:
8 Intercomparison of formaldehyde measurements at the atmosphere simulation chamber SAPHIR,
9 Atmos. Chem. Phys., 8, 2189-2200, 2008.

10 Yokelson, R. J., Burling, I. R., Gilman, J. B., Warneke, C., Stockwell, C. E., de Gouw, J., Akagi,
11 S. K., Urbanski, S. P., Veres, P., Roberts, J. M., Kuster, W. C., Reardon, J., Griffith, D. W. T.,
12 Johnson, T. J., Hosseini, S., Miller, J. W., Cocker, D. R., Jung, H., and Weise, D. R.: Coupling
13 field and laboratory measurements to estimate the emission factors of identified and unidentified
14 trace gases for prescribed fires, Atmos. Chem. Phys., 13, 89-116, 10.5194/acp-13-89-2013, 2013.

15

16

17

Table 1. Summary of the ISAF instrument capability

Size	38 x 43 x 60 cm ³
Weight	25 kg
Power	200 W
Precision	20 pptv/s
Time response	<0.2 s
Accuracy	±10%
Data rate	1s (100 ms on request)
Operation on the DC8 uses pump (10 kg + 300W) and a control interface box (10 kg)	
Operation on the P3 and GV uses pump (5 kg + 200W) and a control interface box (10 kg)	

18

19

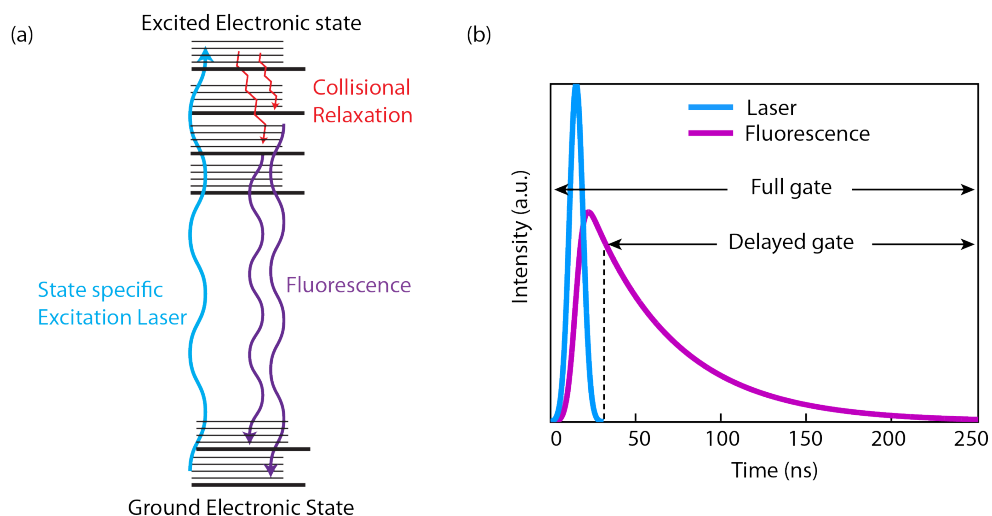
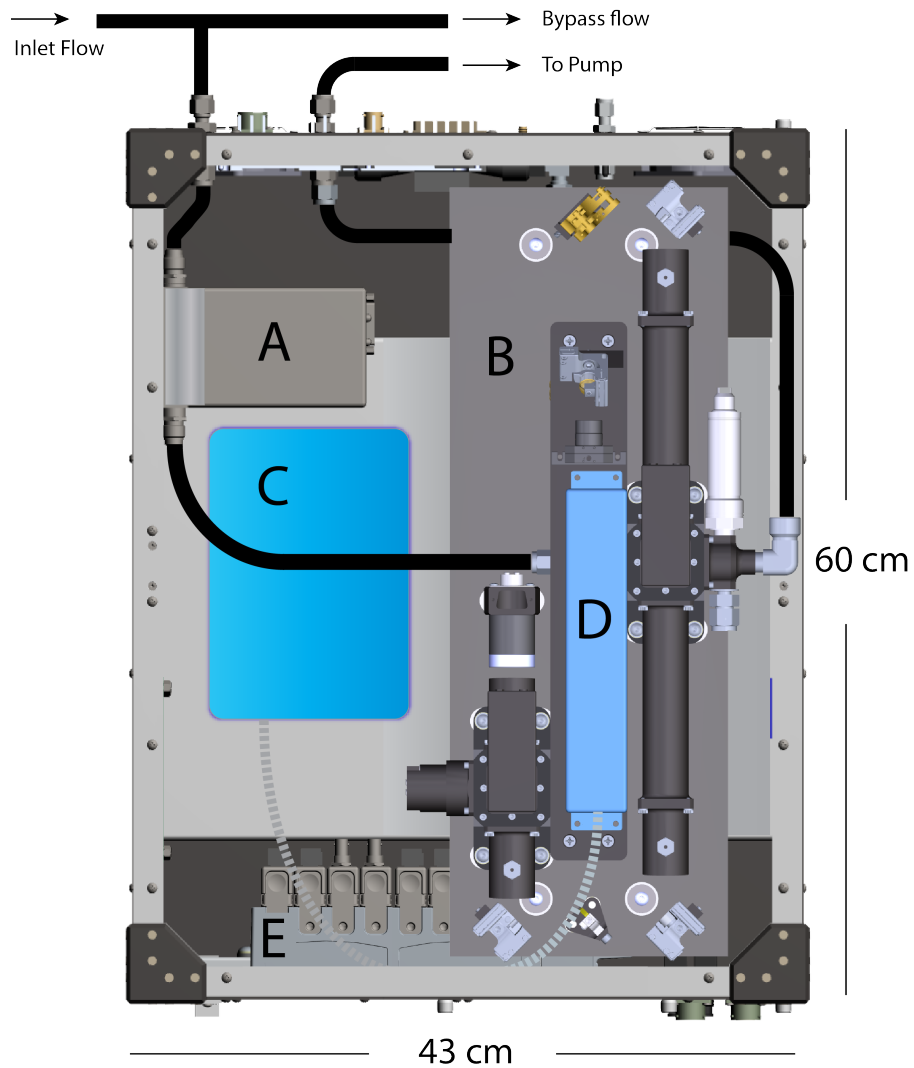


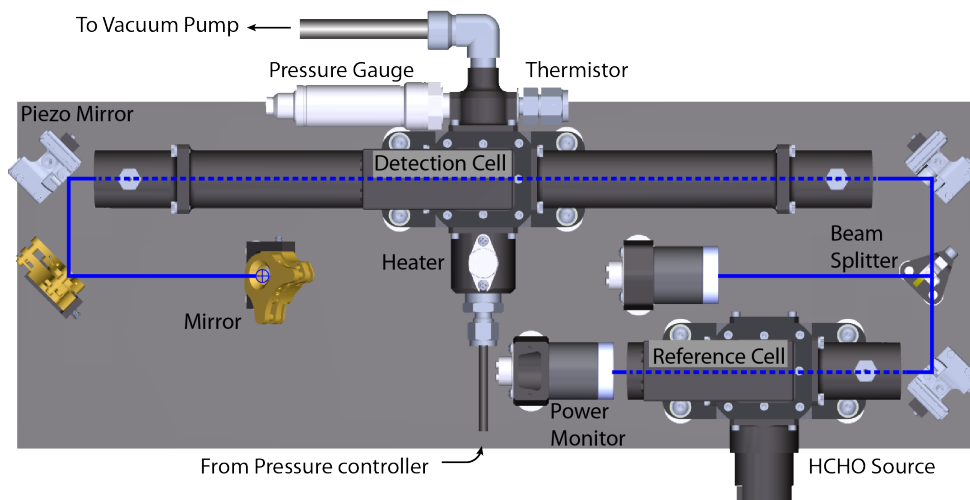
Figure 1. The spectral (a) and temporal (b) features of laser induced fluorescence detection. In (a) the laser excites a single rotational transition at 353.16 nm. The fluorescence occurs after collisional relaxation and appears at longer wavelengths. In (b) time gating of fluorescence detection provides additional discrimination between prompt and longer time-scale processes. Laser excitation and elastic scattering processes that include Raman, Rayleigh and chamber reflections have time-scales that match the laser pulse (25 ns full-width). Fluorescence has a lifetime of 10's of ns and the signal extends for more than 100 ns beyond the end of the laser pulse and elastic scattering. The delayed gate captures HCHO fluorescence while the full gate captures both fluorescence and scattered light.



1

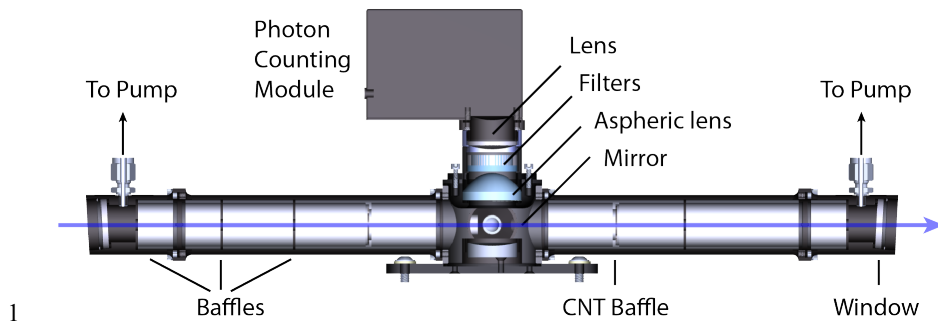
2 Figure 2. A top view of the ISAF instrument layout. The instrument chassis is 60 x 43 x 35 cm
 3 and 25 kg. The major subsystems are labeled: (A) pressure controller, (B) optical bench, (C)
 4 tunable fiber laser, (D) harmonic generation housing, and (E) data acquisition system.

5

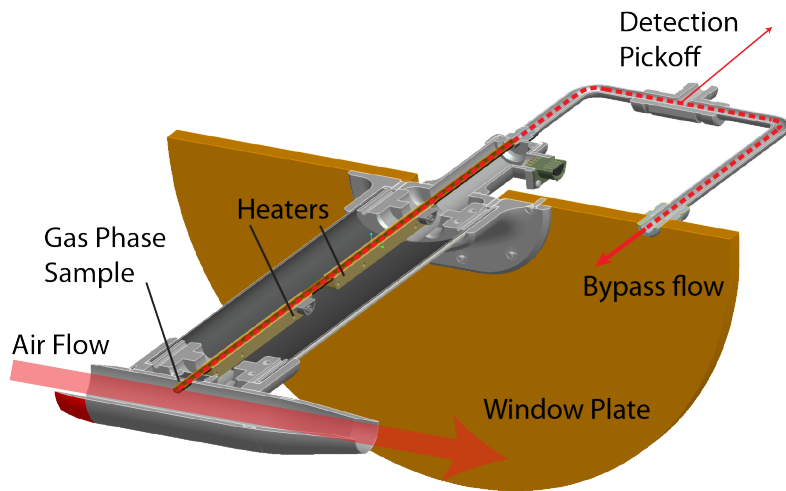


1
2
3
4
5
6

Figure 3. This diagram shows a top view of the optical bench with the harmonic generation housing and platform removed. The laser propagation is indicated by the solid (open to air) and dashed (inside the cells) lines.

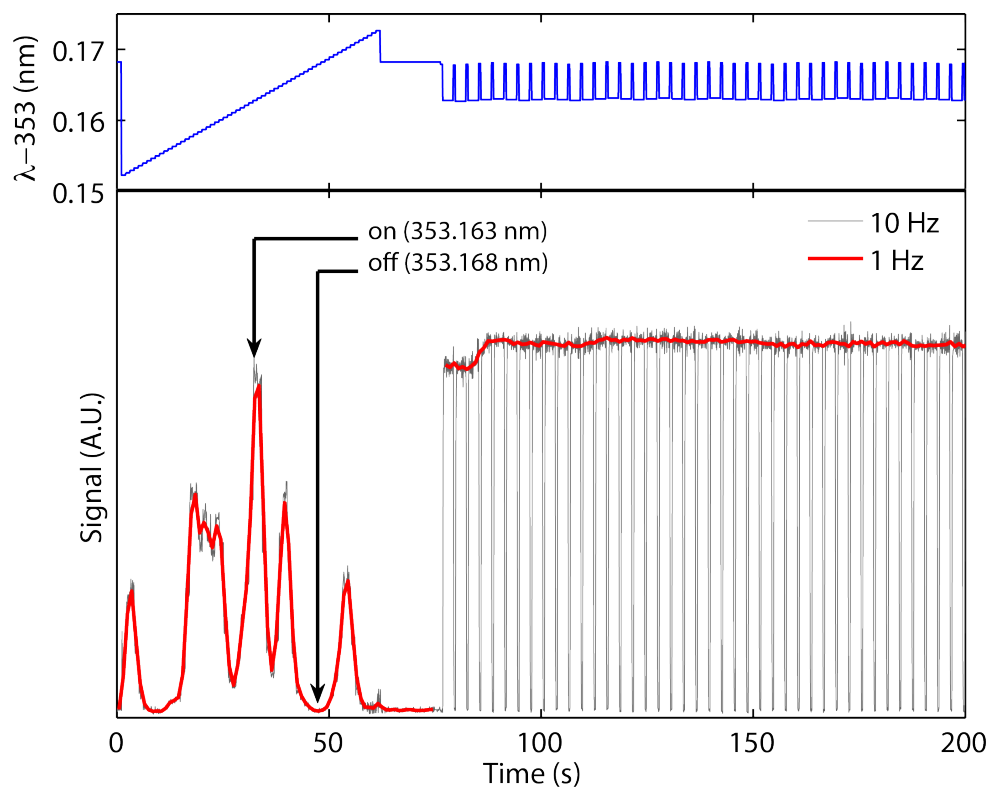


1
2 Figure 4. This diagram shows a side-view of the cross-section of the detection cell. The line
3 indicates the laser path and propagation direction.
4



1
2
3
4
5
6
7
8
9

Figure 5. This diagram shows a cross-section view of the particle rejection inlet mounted on a window plate. A ram air nacelle mounted on an airfoil 30 cm from the plate generates ram pressure that directs the ambient air through the heated tube mounted at 90° to the flow. A small fraction (2 slm) of the heated air enters the instrument and the remainder (~20 slm) returns to ambient. The plumbing on the cabin side of the window plate is not drawn to scale. There is 1 m of tubing between the inlet and detection pickoff.



1
2
3
4
5
6
7
8

Figure 6. These plots show the wavelength (top) and fluorescence signal (bottom) during a scan of the laser, followed by the standard data acquisition mode. The computer algorithm uses the reference cell signal to maintain the laser on the large rotational feature at 353.163 nm. The contributions of species other than HCHO to the fluorescence signal are removed by subtracting the signal at the offline position. The difference between the signal at the online position and the offline position is proportional to [HCHO].

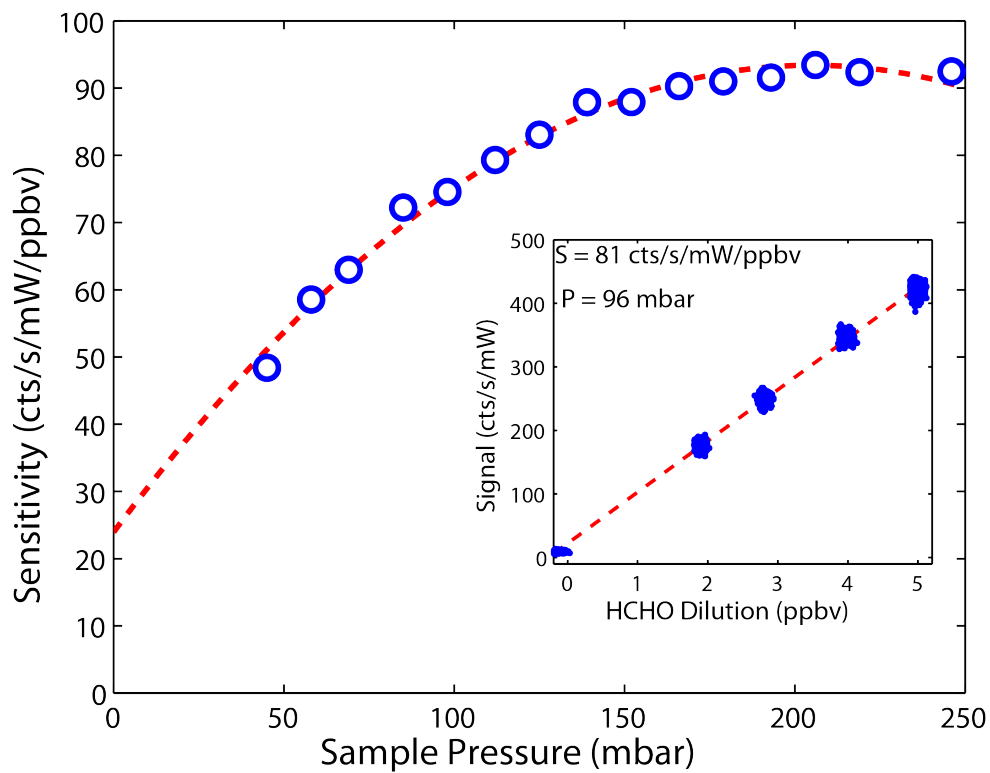
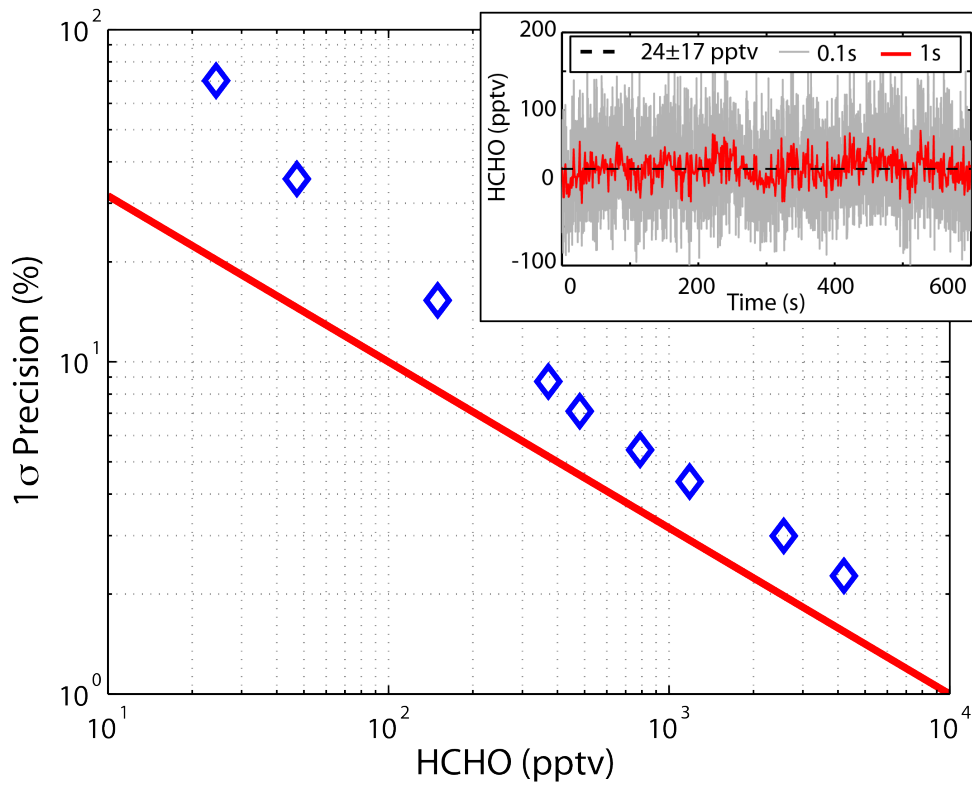


Figure 7. This plot shows the sensitivity of the instrument to HCHO versus pressure. The inset shows an example of a calibration using an HCHO standard addition to a flow of air. Several calibrations at one pressure are used to determine the pressure dependence.



1
2
3
4
5
6
7

Figure 8. This plot shows the measured and theoretical 1- σ precision as a percentage of HCHO concentration. The inset shows an example of the mean and standard deviation for constant HCHO. The average value (24 pptv) and the standard deviation (17 pptv) are used to determine the measured precision (70% in this case) shown by the blue diamonds. The solid line is the theoretical maximum precision based on the counting statistics of the signal level.

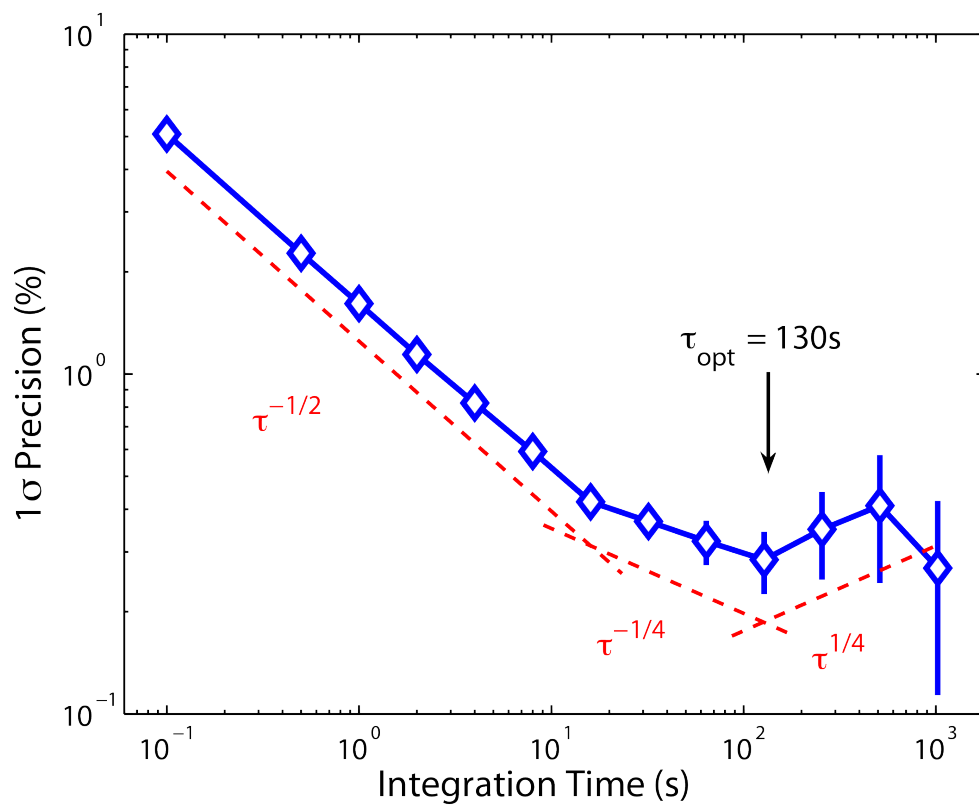


Figure 9. The mean normalized Allen deviation is shown for 60 minutes of sampling at a constant HCHO concentration of 5.1 ppbv. The short integration times show a $\tau^{1/2}$ increase in precision, consistent with white noise.

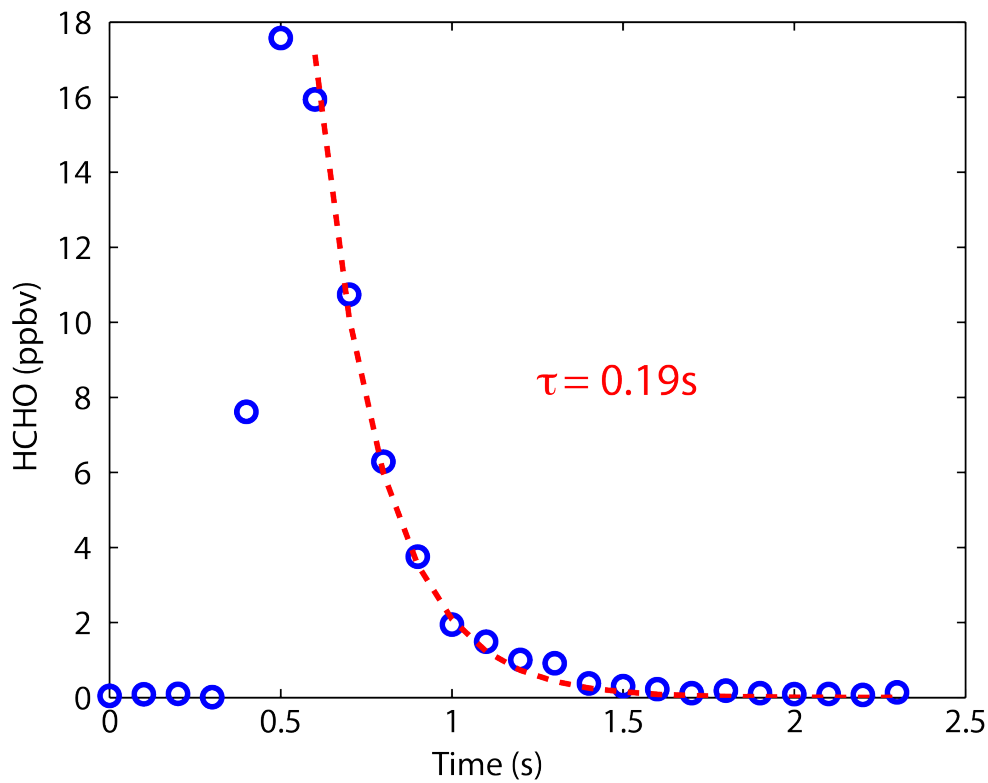
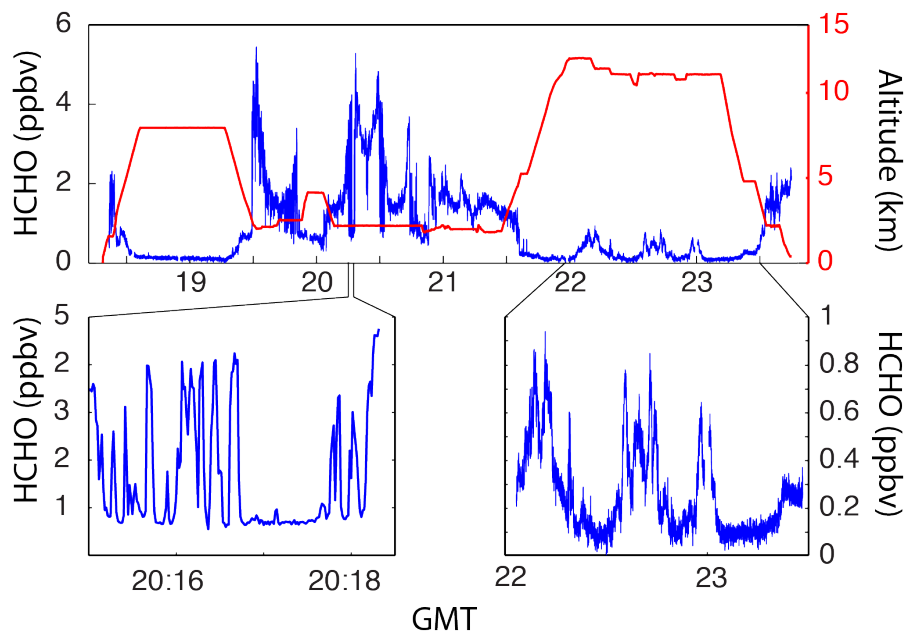


Figure 10. The time response of the instrument is demonstrated with a 10 ms pulse of HCHO added to the sample air flow in the lab. The measured HCHO shows the rapid rise expected with the flush time of ~115 ms. The decay of 190 ms indicates second-order effects such as wall interactions and the presence of small volumes with longer flush times.



1
2
3
4
5
6
7
8

Figure 11. In situ measurements of HCHO are shown for the flight of June 2 on the NASA DC8 during the DC3 campaign in 2012. The top shows 1s HCHO and GPS altitude. The lower portions are expanded views of the boundary layer (BL) leg and the upper tropospheric (UT) leg. The fast response to large changes in ambient HCHO are evident in the BL leg. The sensitivity (better than 20 pptv/s) is evident in the UT leg.

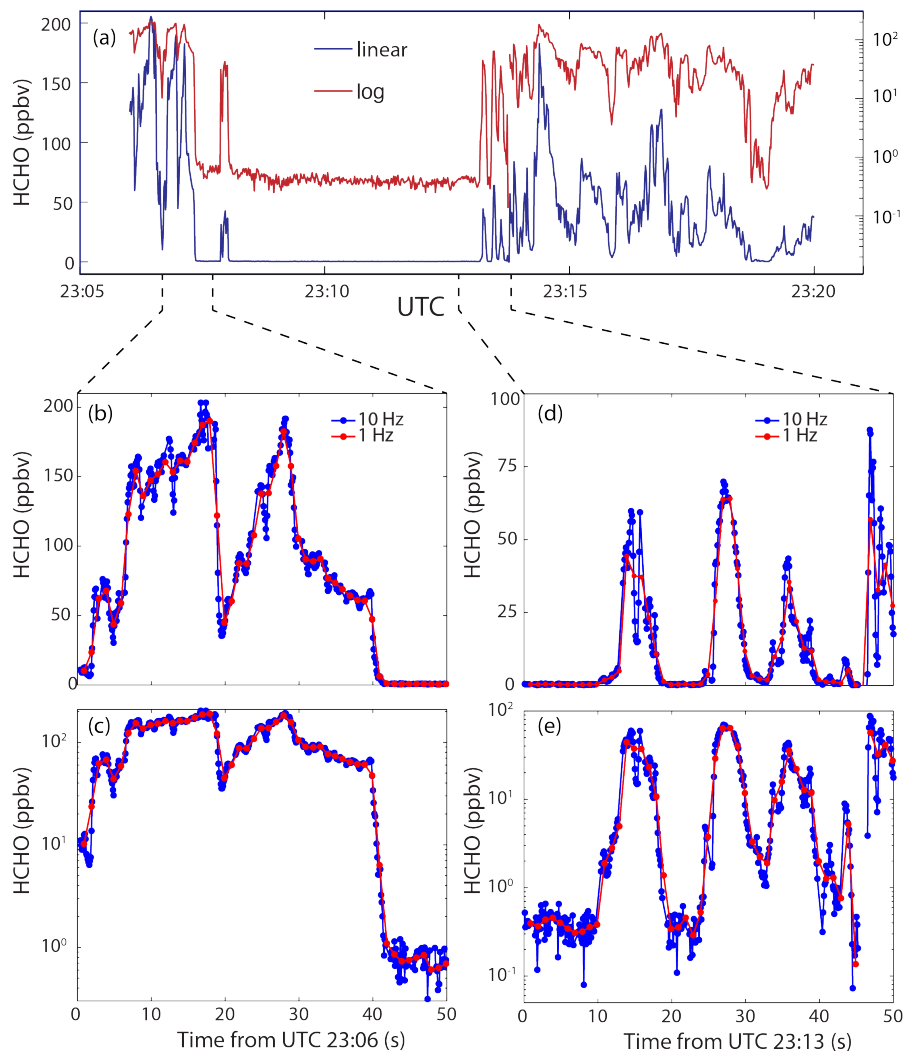


Figure 12. The time series obtained during the SEAC4RS campaign on the NASA DC8 on August 26, 2013. The panel (a) shows the HCHO measured at a constant pressure altitude of 5 km as the DC8 sampled the plume from the Ring Fire in Yosemite National Park as the plume travelled eastward over California and Nevada. Note the linear and logarithmic scaling. Panels (b) and (c) show a window of 50 seconds starting at UTC 23:06 expanded with data averaged at 10 Hz and 1 Hz for linear and logarithmic scaling. Panels (c) and (d) show the same for the 50 s window starting at UTC 23:13.